

# Numerical Simulation of Unsteady Combustion Using the Transport Element Method

Marios C. Soteriou  
Dept. of Mechanical Engineering  
University of Connecticut  
Storrs, CT 06269-3139, USA

Ahmed F. Ghoniem  
Dept. of Mechanical Engineering  
Massachusetts Institute of Technology  
Cambridge, MA 02139, USA

## Abstract

The transport element method is described and implemented in the simulation of the non-premixed reacting shear layer. The method, a natural extension of the vortex element method, resolves the low Mach number variable density flow and the exothermic reacting field. The effect of combustion on the flow is accommodated by incorporating a volumetric expansion velocity component and by modifying the integration of the vorticity equation to include expansion-related and baroclinic terms. The reacting field equations describing a single step, irreversible, chemical reaction, are simplified by the introduction of Schvab-Zeldovich (SZ) conserved scalars whose transport is sufficient to compute the evolution of combustion in the case of infinite reaction rate. In the case of finite rate chemistry the evolution of one primitive scalar, the product mass-fraction, is also computed. The vorticity, conserved scalar gradient and product mass fraction are discretized amongst fields of transport elements. Their time evolution is implemented by advecting the elements at the local velocity while simultaneously integrating their transport equations along particle trajectories. The integration of the vorticity and the conserved scalar gradient equations is simplified using ideas from kinematics. A novel core expansion scheme that avoids the problems associated with the conventional implementation is used to simulate diffusion. Field quantities are obtained using convolutions over the elements. Results indicate that the method is able to accurately reproduce the essential features of the flow. Convergence of the solution in time is approximately linear. Moreover, the finite reaction rate solution at low Karlovitz number bear strong similarities to that of the infinite reaction rate model. This similarity is exploited in validating the part of the numerical methodology related to the integration of the product mass-fraction equation.

## 1 Introduction

Generalization of the vortex element method (VEM) [3] by incorporating the physics of scalar transport, mixing and reaction, has been an ongoing effort since the inception of the method [4, 7, 8, 10, 14–16, 19]. The essential features of this process; the discretization of primitive variable gradients, their Lagrangian transport and use of flow kinematics to monitor their evolution, offer significant advantages in the simulation of reacting flows. The simulation of these flows involves substantial complexities. These include the presence and continuous mixing of many species, the evolution of temporal and spatial scales which cover several decades, the presence of strongly non-linear and coupled phenomena and the coupling of the combustion energy release and the associated changes in the density and transport properties and the flow. The latter requires the modification of VEM which in its basic form deals with incompressible uniform density flow. Moreover, reacting flows are characterized by thin reaction fronts, i.e. regions of sharp scalar gradients, which evolve in a highly convoluted manner.

Early attempts to simulate reacting flows using a VEM-based approach simplified the reacting field through the use of flame sheet models. In these [7] and [8], the sharpness of the flame front was exploited to represent it as a sheet which encompasses the reaction and diffusion regions of the flame and separates unmixed scalars. The effects of combustion on the flow were restricted to those associated with the volumetric expansion by distributing volumetric sources along the flame sheet.

To move beyond these simplified models, one needs a detailed description of the mixing field as a first step in the accurate representation of the reacting field. This was accomplished by the development of the transport element method (TEM) in two [16, 19] and three dimensions [14]. The TEM bears substantial similarities to the VEM to which it is fully compatible. Essentially, it discretizes the scalar-gradients and evolves them by using information from the kinematics of material lines. The scalars are obtained from the gradients via convolutions over their fields. A version of the TEM incorporating reaction in a two-dimensional temporally evolving flow was also proposed [10]<sup>1</sup>. Its implementation, however, in the spatially developing model of the flow is not, in general, possible. The reason for this lies in the temporal model, which due to its utilization of periodic boundary conditions represents a mathematical idealization of the flow it attempts to represent<sup>2</sup>. The TEM as presented in [10] takes full advantage of the simplifications offered by the temporal model and, as a result, cannot be applied in spatially developing flows.

In this work, we present a new version of TEM which is applicable to spatially developing flows. Through the introduction of SZ variables, the method is able to use a combination of scalar-gradients and a primitive scalar to completely describe the reacting field. Combustion energy release effects on the flow, at low Mach number, are captured using the variable density version of the VEM.

## 2 Formulation

A two-dimensional flow is considered. Compressibility effects are restricted to the low Mach-number limit. Combustion follows a single-step reaction which consumes two reactants, one from each stream, to form a single product according to an Arrhenius mechanism. All species behave as perfect gases with equal molecular weights and equal and constant specific heats and mass diffusivities. The Lewis number is equal to unity and molecular diffusion is relatively small, i.e., the flow is at high Reynolds and Peclet numbers<sup>3</sup>. Accordingly, the non-dimensionalized governing equations are:

$$\frac{d\rho}{dt} + \rho \nabla \cdot \mathbf{u} = 0; \quad (1)$$

---

<sup>1</sup>A three dimensional scheme was also proposed [4, 15] but one in which the scalar-gradient approach was abandoned in favor of a primitive scalar one and temperature independent kinetics was assumed.

<sup>2</sup>The limitations of the temporal model in the simulation of reacting flows exceed those for the non-reacting flow which have been pointed out previously [5]. By construction, the temporal model is valid only for very small and very large values of the Karlovitz number. The first, represents very fast combustion characterized by thin continuous flames, while for the second, gaseous fuel combustion is unsustainable. Irrespective of the numerical method used, the model's implementation to flows of moderate Karlovitz number in which interaction of the flow and reaction time scales is experienced and sharply transient phenomena such as quenching, and re-ignition take place is problematic.

<sup>3</sup>Most of the assumptions related to the reaction model are employed to reduce the computational effort and are not imposed by a fundamental limitation in the numerical scheme (Section 3). An exception to this is the equal diffusivities assumption which enables the use of the Schvab-Zeldovich formulation. The diffusivities, however, do not necessarily have to be constant. Moreover, a larger number of species may be considered and the molecular masses may be unequal as long as it is assumed that the diffusivities are not similarly affected. This approach was followed in the implementation of the methodology presented herein for the simulation of the axisymmetric buoyant plume [17].

$$\frac{d\mathbf{u}}{dt} = -\frac{\nabla p}{\rho} + \frac{1}{Re} \nabla^2 \mathbf{u}; \tag{2}$$

$$\frac{ds_j}{dt} = \frac{1}{Pe} \nabla^2 s_j + Q_j \frac{\dot{w}}{\rho} \tag{3}$$

with

$j$	1	2	3	4 <sup>(+)</sup>
$s_j$	$T$	$Y_f$	$Y_o$	$Y_p$
$Q_j$	$Q_o$	-1	$-\phi$	$1 + \phi$

while  $\rho T = 1$ ;  $\eta_f + \phi^* \eta_o \rightarrow (1 + \phi^*) \eta_p$ ,  $Y_f + Y_o + Y_p = 1$  and  $\dot{w} = A_f \rho^2 Y_f Y_o \exp(-\frac{T_a}{T})$ . In the above:  $\mathbf{u} = (u, v)$  is the velocity vector in a right-handed Cartesian coordinate system  $\mathbf{x} = (x, y)$ ,  $t$  is time,  $\nabla = (\frac{\partial}{\partial x}, \frac{\partial}{\partial y})$  is the gradient operator,  $\frac{d}{dt} = \frac{\partial}{\partial t} + \mathbf{u} \cdot \nabla$  the material derivative,  $p$  is the pressure,  $\rho$  and  $T$  are the fluid mixture density and temperature respectively, subscripts  $f, o$  and  $p$  indicate the fuel, oxidizer and product, respectively,  $\eta_i$  denotes species  $i$ ,  $i = f, o, p$ ,  $Y_i$  is the mass-fraction for species  $i$ ,  $\dot{w}$  is the reaction rate,  $Re$  and  $Pe$  are the Reynolds and Peclet numbers, respectively,  $A_f, Q_o$  and  $T_a$  are the non-dimensionalized frequency factor, enthalpy of reaction, and activation temperature, respectively, and  $\phi^*$  and  $\phi$  are the molar and mass stoichiometry ratios, respectively.

The equations are transformed into vorticity-gradient form, and the velocity is decomposed into a vorticity-induced solenoidal component,  $\mathbf{u}_\omega$ , and two irrotational components;  $\mathbf{u}_e$  due to volumetric expansion, and  $\mathbf{u}_b$  due to the boundary conditions:

$$\mathbf{u} = \mathbf{u}_\omega + \mathbf{u}_b + \mathbf{u}_e \tag{4}$$

$\mathbf{u}_\omega$  is obtained from the definition of the vorticity and by using a streamfunction,  $\psi$ , i.e.

$$\nabla^2 \psi = -\omega, \quad \mathbf{u}_\omega = \nabla \times (\psi \hat{\mathbf{k}}) \tag{5}$$

where  $\hat{\mathbf{k}}$  is the unit vector normal to the plain of motion. The irrotational components are obtained from the continuity equation by introducing two velocity potentials,  $\Phi$ , such that

$$\nabla^2 \Phi_e = -\frac{1}{\rho} \frac{d\rho}{dt}, \quad \mathbf{u}_e = \nabla \Phi_e \tag{6}$$

and

$$\nabla^2 \Phi_b = 0, \quad \mathbf{u}_b = \nabla \Phi_b \tag{7}$$

The evolution of the vorticity is described by taking the curl of Eq. 2:

$$\frac{d\omega}{dt} \hat{\mathbf{k}} + (\nabla \cdot \mathbf{u}) \omega \hat{\mathbf{k}} = \frac{\nabla \rho \times \nabla p}{\rho^2} + \frac{1}{Re} \nabla^2 \omega \hat{\mathbf{k}}. \tag{8}$$

For the scalar transport equations, Schvab-Zeldovich (SZ) conserved variables,  $\lambda$  and  $\gamma$ , are introduced such that:

$$\lambda = Y_o - \phi Y_f, \quad \gamma = T - \frac{Q_o}{1 + \phi} Y_p. \tag{9}$$

These variables are constructed such that their governing equations are devoid of reaction source terms. The resulting SZ convection-diffusion equations have equal diffusivities and same type of boundary conditions and can thus be reduced to a single equation via appropriate scaling:

$$\frac{d\beta}{dt} = \frac{1}{Pe} \nabla^2 \beta, \quad \text{where} \quad \beta = \frac{\lambda - \lambda_2}{\lambda_1 - \lambda_2} = \frac{\gamma - \gamma_2}{\gamma_1 - \gamma_2} \tag{10}$$

and  $\lambda_1, \lambda_2, \gamma_1, \gamma_2$  are the scaling values<sup>4</sup>.

In analogy to the treatment of the flow equations, the SZ scalar transport equation is recast into gradient form:  $\mathbf{g} = \nabla\beta$

$$\frac{d\mathbf{g}}{dt} + \mathbf{g} \cdot \nabla\mathbf{u} + \mathbf{g} \times (\omega\hat{\mathbf{k}}) = \frac{1}{Pe}\nabla^2\mathbf{g}. \quad (11)$$

When the reaction rate is finite reactants do not coexist and the reaction zone collapses onto a line. Under these conditions the distributions of the SZ variables provide a complete description of the reacting field *without the need for the solution of a reacting scalar*. The reaction interface is trivially established as the locus of  $\lambda = 0$ , while

$$\lambda \geq 0 : Y_f = 0, Y_o = \lambda, Y_p = 1 - \lambda$$

and

$$\lambda \leq 0 : Y_f = -\frac{\lambda}{\phi}, Y_o = 0, Y_p = 1 + \frac{\lambda}{\phi}.$$

When the reaction rate is infinite, the complete description of the scalar field requires the solution of one reacting scalar, e.g., the product mass-fraction and

$$Y_f = \frac{-\lambda + (1 - Y_p)}{1 + \phi}, \quad Y_o = \frac{\lambda + \phi(1 - Y_p)}{1 + \phi}, \quad T = \gamma + \frac{Q_o}{1 + \phi}Y_p.$$

### 3 Numerical scheme

*Discretization:* The vorticity, expansion source,  $-\frac{1}{\rho}\frac{d\rho}{dt}$ ,  $\beta$ -gradient and product-mass-fraction are represented by a generic discretization function. Thus, a property  $\zeta$  is discretized among a number of elements characterized by a finite area,  $A_i$ , and strength,  $\zeta_i$ , locally distributed according to a radially-symmetric core function,  $f_\delta$ . The discretization function is also used to reconstruct the discretized quantities at later times. In particular;

$$\zeta(\mathbf{x}, t) = \sum_{i=1}^N \zeta_i(t)A_i(t)f_\delta(|\mathbf{x} - \boldsymbol{\chi}_i|), \quad (12)$$

where  $\boldsymbol{\chi}_i = \boldsymbol{\chi}_i(\mathbf{x}, t)$  is the element location. The core function, characterized by the core radius  $\delta$  within which the most significant contribution of each element is concentrated, is a second-order Gaussian:  $f_\delta = \frac{1}{\pi\delta^2}\exp(-r^2/\delta^2)$  which leads to second-order accuracy when core overlap among neighboring elements is maintained [12].

Discretization may follow one of two approaches. In the first,  $\zeta_i$  are found from Eq. 12. This yields high discretization accuracy at the cost that the element strengths do not necessarily have a physical meaning but are merely weights of an interpolation function. It is not, therefore, obvious that the strengths should be governed by the same transport equations as the properties they are used to represent. This is particularly the case when transport equations which involve source terms are considered.

In the second approach,  $\zeta_i = \zeta(\boldsymbol{\chi}_i)$ . This alleviates the problem encountered in the first approach but at the cost of reduced discretization accuracy<sup>5</sup>. It is found, however, that if the discretized

<sup>4</sup>In the case of the shear layer flow the scaling values are those of the two free streams—see Section 4. It should also be noted that when the two scaling values of a given property are equal then its field distribution is trivially reduced to a constant.

<sup>5</sup>The discretization accuracy in this case is a strong function of the overlap of the cores, generally decreasing as the overlap increases.

field is subsequently integrated, as is the case for the vorticity and the  $\beta$ -gradient, the error in the integrated quantity, i.e. the velocity and the scalar, respectively, is much smaller<sup>6</sup>. For this reason, in this work, this second approach is followed for the vorticity and the  $\beta$ -gradient. For the product mass-fraction, for which no integration of the solution is needed, an approach similar to the first is implemented but which does not involve the drawback mentioned. Details of this approach are given in the section dealing with the integration of the transport equations.

*Calculation of the velocity and scalar fields:* This essentially entails the solution of a number of Poisson and Laplace equations. For the former, Green's function based solutions are invoked, while for the latter conformal mapping techniques are implemented.

The Green's function solution of Eq. 5 for the streamfunction and the subsequent differentiation for the velocity are lumped into one step to yield a Biot-Savart convolution. Using the discrete vorticity field Eq. 12, we get

$$\mathbf{u}_\omega(\mathbf{x}, t) = \sum_{i=1}^N \Gamma_i(t) \mathbf{K}_\delta(\mathbf{x} - \boldsymbol{\chi}_i(t)), \quad (13)$$

where  $\Gamma_i(t) = \omega_i(t)A_i(t)$  is the element circulation  $\mathbf{K}_\delta(\mathbf{x}) = \overline{\mathbf{K}}(\mathbf{x})F(\frac{r}{\delta})$ , where  $\overline{\mathbf{K}}(\mathbf{x}) = -(y, -x)/(2\pi r^2)$  and  $F(r) = 2\pi \int_0^r r f(r) dr = 1 - \exp(-r^2)$ .

A similar approach is followed in the solution of Eq. 6. The calculation of the expansion potential, like that of the streamfunction, is bypassed via a convolution which directly relates the expansion-source to the expansion velocity. A desingularized equivalent of this convolution is obtained using the assumed expansion-source field Eq. 12, and is:

$$\mathbf{u}_e(\mathbf{x}, t) = - \sum_{i=1}^N \left( -\frac{1}{\rho} \frac{d\rho}{dt} \right)_i (t) A_i(t) \nabla G_\delta(\mathbf{x} - \boldsymbol{\chi}_i(t)), \quad (14)$$

where

$$\nabla G_\delta(\mathbf{x}) = \nabla \overline{G}(\mathbf{x}) F\left(\frac{r}{\delta}\right) \quad \text{and} \quad \nabla \overline{G}(\mathbf{x}) = -\frac{(x, y)}{2\pi r^2}$$

The velocity induced by the boundary conditions is obtained from Eq. 7 using Schwartz-Christoffel conformal mapping and the method of images (Section 4).

The  $\beta$  SZ scalar solution is obtained from the corresponding gradient field by recognizing that scalar and gradient can also be related via a Poisson equation,  $\nabla^2 \beta = \nabla \cdot \mathbf{g}$ . The Green's function solution of this equation is further manipulated by performing a by-parts integration, using the divergence theorem and recognizing that the gradient field decays at infinity (unbounded domain):  $\beta(\mathbf{x}) = \int \nabla \overline{G}(\mathbf{x} - \mathbf{x}') \cdot \mathbf{g}(\mathbf{x}') d\mathbf{x}'$ . Using the gradient field of Eq. 12 a discrete desingularized form is obtained:

$$\beta(\mathbf{x}, t) = \sum_{i=1}^N \mathbf{g}_i A_i(t) \cdot \nabla G_\delta(\mathbf{x} - \boldsymbol{\chi}_i(t)) + \beta_b. \quad (15)$$

$\beta_b$  here is the integration related function. It is determined using a Schwartz-Christoffel conformal mapping while satisfying the boundary condition using images.

*Integration of the transport equations:* The time evolution of the flow and scalar fields is established by numerically integrating the transport equations locally for each element. For this purpose, the

---

<sup>6</sup>A reduction of one order of magnitude (from about 5% to 0.1%) in the maximum pointwise discretization error was experienced between a Gaussian vorticity and the corresponding errorfunction velocity profiles.

integration takes place in two fractional steps [2], the first deals with all processes other than diffusion, while the second concentrates on the latter.

During the first step the element location is updated by numerically integrating

$$\frac{d\boldsymbol{\chi}_i}{dt} = \mathbf{u}(\boldsymbol{\chi}_i, t) \quad (16)$$

using a predictor-corrector scheme. This defines element trajectories and material lines.

The element vorticity is updated by integrating the circulation equation:

$$\frac{\Gamma_i(t)}{dt} = -\frac{[\nabla\rho]_i(t)}{\rho(\boldsymbol{\chi}_i, t)} \times \frac{d\mathbf{u}(\boldsymbol{\chi}_i, t)}{dt} A_i(t), \quad (17)$$

where the pressure gradient has been replaced by the material acceleration using the momentum equation. The integration is accomplished using a predictor-corrector scheme in which the material acceleration is established via a two-step iteration, forward-difference algorithm. Equation 17 is obtained from the vorticity equation using kinematics<sup>7</sup>.

Using kinematics to simplify the transport is also followed in the integration of the  $\beta$ -gradient transport equation. The first fractional step in the integration of this equation describes pure convection. Recognizing that in such a case isoscalar and material lines coincide and considering the kinematical evolution of the latter in conjunction with continuity we can rewrite the governing transport equation<sup>8</sup> (left hand side of Eq. 15) as

$$\frac{d}{dt} \left[ \frac{g_i(t)}{\rho(\boldsymbol{\chi}_i, t) dl_i(t)} \right] = 0, \quad (18)$$

with  $\mathbf{g}_i = g_i \hat{\mathbf{n}}_i$  and  $dl_i = |\mathbf{dl}_i|$ , where  $\hat{\mathbf{n}}_i$  is the unit vector normal to the material line and  $\mathbf{dl}_i$  is a material line elemental segment. Equation 18 implies that  $\frac{g_i(t)}{\rho(\boldsymbol{\chi}_i, t) dl_i(t)} = \text{constant}$  along a material-isoscalar line. The constant is specified by the initial conditions, and  $\mathbf{dl}_i$  as well as  $\hat{\mathbf{n}}_i$  are readily available due to the Lagrangian nature of the scheme.

When the reaction rate occurs at infinite rate, integration of Eqs. 16–18 completes the first fractional integration step. For the general, finite reaction rate case, however, the integration of the product mass-fraction transport equation is also carried out. In this case, the concept of product particles is introduced. These particles are located at the element centers and directly experience the reaction process. The need to use these particles stems from the fact that the nonlinearity of the reaction requires the use of precise values for the properties involved in the reaction rate. As already seen, the strengths of the elements are crude approximations of the values of the field properties at the same location. Implementing reaction on the element strength will yield erroneous, even non-physical results. In addition, depending on the diffusion algorithm to be used, the strengths may not experience the diffusion process (e.g. in the traditional expanding core [18], the random walk [3] or the diffusion velocity [13] schemes). Since only material which mixes molecularly can burn, the use of the strengths for reaction will unavoidably lead to errors<sup>9</sup>.

<sup>7</sup>Material line kinematics expressed in the form  $\frac{d(\mathbf{dl})}{dt} = \mathbf{dl} \cdot \nabla \mathbf{u}$ ,  $\mathbf{dl}$  being a material line elemental segment, combined with continuity equation yields  $\nabla \cdot \mathbf{u} = \frac{1}{dA} \frac{d(dA)}{dt}$  where  $dA = dl dn$  is an elemental fluid element area with  $dl$  and  $dn$  being the element's dimensions along and normal to the material line, respectively. Substituting this expression into the vorticity equation and assuming that the vorticity is constant over the area of the fluid element yields:  $\frac{d\omega}{dt} + (\nabla \cdot \mathbf{u})\omega = \frac{1}{dA} \left( dA \frac{d\omega}{dt} + \frac{d(dA)}{dt} \omega \right) = \frac{d(\omega dA)}{dt} = \frac{d\Gamma}{dt}$ .

<sup>8</sup>For derivation see Ref. [16].

<sup>9</sup>In this case, reaction will cease as soon as any originally premixed material (i.e. from initial or inlet conditions), burns.

This last point is important in the implementation of diffusion. Problems related to the traditional core expansion scheme are associated with the *transport* of expanded cores during convection [11]. The implementation of diffusion, on the other hand, is exact. With product particles, the expanded cores are not convected. As will be seen, the cores expand during the diffusion step, the new particle values are established, the particles are convected, and then the new interpolation function is created using the original size cores. The net result of this is that the long term effect of diffusion is to change the strengths of the elements rather than the cores. In this respect the version of the core expanding scheme presented here bears similarities to the particle exchange scheme of diffusion [6]<sup>10</sup>.

The integration of the product mass-fraction equation, like that of the rest of the transport equations, is carried out in two fractional steps. In the first step we integrate:

$$\frac{Y_p(\boldsymbol{\chi}_i, t)}{dt} = (1 + \phi)\dot{w}(\boldsymbol{\chi}_i, t), \quad (19)$$

for each product particle via an Euler predictor-corrector scheme. This yields the product values prior to diffusion, denoted as  $Y_p^\#(\boldsymbol{\chi}_i, t)$ . These values are used to discretize the product field and obtain the element product strengths as noted earlier, i.e.

$$\sum_{i=1}^N Y_{pi}(t) A_i(t) f_\delta(|\mathbf{x} - \boldsymbol{\chi}_i|) = Y_p^\#(\boldsymbol{\chi}_i, t) \quad (20)$$

The solution of this system of equations is simplified by taking into account the nature of the core-function which implies that only the closest neighbors contribute to the strength of an element. Thus, in establishing the strength of a given element, only elements which are  $r/\delta < \sqrt{12}$  (i.e.  $\exp[-(r/\delta)^2] > 10^{-6}$ ) away from the element are considered. A functional iteration is used in the solution of Eq. 20 which is greatly helped by the availability of good initial guesses, offered by the values of the strengths at the previous time step.

To check the discretization error which by construction is small, and to minimize its effects, the product particle values are reconstructed from the obtained strengths yielding  $Y_p^{\#\#}(\boldsymbol{\chi}_i, t)$  with  $|Y_p^{\#\#}(\boldsymbol{\chi}_i, t) - Y_p^\#(\boldsymbol{\chi}_i, t)|$  being the value of pointwise discretization error.

Subsequently, the diffusion step is performed via the core expansion scheme

$$\delta_i^2(t + \Delta t) = \delta_i^2(t) + \frac{4\Delta t}{C}, \quad (21)$$

where  $C = Re$  for  $\zeta = \omega$  and  $C = Pe$  for  $\zeta = \mathbf{g}$  or  $Y_p$ , which is the analytical solution of the diffusion equation for each element. For the product mass-fraction, one more manipulation is executed to reduce the impact (if any) of the discretization error.

Clearly, the solution after the diffusion step,  $Y_p^{\#\#D}(\boldsymbol{\chi}_i, t)$ , includes this error. By subtracting the discretization error from this solution, a new, corrected, solution is obtained

$$Y_p(\boldsymbol{\chi}_i, t) = Y_p^\#(\boldsymbol{\chi}_i, t) + \Delta Y_p^{\#\#D}(\boldsymbol{\chi}_i, t) \quad (22)$$

where  $\Delta Y_p^{\#\#D}(\boldsymbol{\chi}_i, t) = Y_p^{\#\#D}(\boldsymbol{\chi}_i, t) - Y_p^{\#\#}(\boldsymbol{\chi}_i, t)$  which includes discretization error only in the change of the product particle field due to diffusion  $\Delta Y_p^{\#\#D}(\boldsymbol{\chi}_i, t)$ . Since the physical problem definition specifies the diffusion to be small, this approach allows even significant discretization errors to be tolerated. In this work, however, this effect was not exploited and the average discretization error was kept smaller than 1%. The reason is that while the discretization error is

<sup>10</sup>We are indebted to Dr. Georges-Henri Cottet for pointing this out during a recent discussion.

subtracted from the product particle solution ( $Y_p(\boldsymbol{\chi}_i, t)$ ) it is not removed from the product field solution ( $Y_p(\mathbf{x}, t)$ ) since it is still included in the product strengths. Thus, while the error is not fed back into the Lagrangian calculations (i.e. the integration of the product equation) it is present in any instantaneous spatial product field evaluation.

The calculation of the density gradient necessary in the integration of the circulation equation implies knowledge of the product mass-fraction gradient field. In the infinite reaction rate case this is trivially established from the SZ gradients. For the finite reaction rate, it is established by differentiating the product mass-fraction field given by Eq. 18 as suggested by Anderson [1], i.e.

$$\nabla Y_p(\mathbf{x}, t) = \sum_{i=1}^N Y_{pi}(t) A_i(t) \nabla f_\delta(\mathbf{x} - \boldsymbol{\chi}_i). \quad (23)$$

The severe stretching of the Lagrangian mesh used in the discretization of the transported quantities, which increases the distance between neighboring elements, may lead to the deterioration of the solution accuracy. To overcome this problem, a scheme of local mesh refinement is adopted, based on local conservation principles, whereby elements are continuously introduced and deleted to ensure core overlap [9].

## 4 Geometry and boundary conditions

The computational domain and some boundary conditions are shown in Fig. 1. The shear layer evolves in a two-dimensional channel of height  $H$  and length  $X_{\max}$ , between two parallel streams (1 top, 2 bottom) which mix downstream of a thin splitter plate. Initially, both streams are at the same temperature and density,  $T_o$ ,  $\rho_o$ , and each carries a single reactant. The top and bottom walls are modeled as rigid, free slip, impermeable and adiabatic planes. At the downstream section, a condition of vanishing vorticity and scalar gradient is used as outflow boundary condition, and is applied by removing the elements which cross the exit boundary. The error introduced by this rather arbitrary exit boundary condition was investigated by performing simulations with increasingly longer domains and quantitatively comparing the solution in their common sections. An example from this study is shown in Fig. 3 which presents results of simulations of the forced non-exothermic flow for  $X_{\max} = 7$ , top, and  $X_{\max} = 5$  bottom. The shear layer is represented by plotting the transport elements and their local velocity vectors relative to the mean flow<sup>11</sup>. We found that the difference between the two solutions was negligible at about one channel width upstream from the exit of the shorter domain (left dashed line in Fig. 3).

The inlet profiles required in the simulation, the vorticity and  $\beta$ -gradient, and, in the case of finite reaction rate, the product mass-fraction, are:

$$\omega(x = 0, y, t) = -\frac{U_1 - U_2}{\sqrt{\pi}\sigma} Z(y), \quad \nabla \beta(x = 0, y, t) = \frac{1}{\sqrt{\pi}\sigma} Z(y), \quad Y_p(x = 0, y, t) = Y_{p_{\max}} Z(y),$$

where

$$Z(y) = \exp\left[-\frac{(y - 0.5)^2}{\sigma^2}\right].$$

In the above expressions, the channel height is the non-dimensionalizing lengthscale, while  $U_1$ ,  $T_o$  and  $\rho_o$  are the velocity, temperature and density scales, respectively.  $\sigma$ , the standard deviation of

<sup>11</sup>The physical and numerical parameters used in obtaining the results of Fig. 2 not specified here are the same as those of the main body of the results of this paper which are given in the following sections.

the Gaussian profiles, is defined by requiring that two wavelengths of the most unstable mode of the uniform density shear layer fit within the channel height ( $\sigma = 0.04$ ).  $Y_{p_{\max}}$  is chosen as 0.4.

The boundary conditions are satisfied by using a Shwartz-Christoffel conformal transformation, which maps the entire channel region onto the upper half of a complex plane (Fig. 2). In this mapping the two fluid streams appear as volume sources symmetrically located with respect to the origin, and solutions to the Laplace equations governing  $\mathbf{u}_b$  and  $\beta_b$  can be simply established by using mass conservation arguments. The mapping however, is also beneficial to the implementation of the image system for the transport elements which helps impose the boundary conditions.

Initialization of the calculation is carried out by assuming that the inlet conditions persist throughout the domain. Hence, within the support of the vorticity,  $\beta$ -gradient and product mass fraction, a square mesh of elements of side  $h = 0.0195$  are distributed along nine material layers. The value of the core radius is  $\delta = 0.0234$ . It is noted that the discretization of the initial profiles may essentially be accomplished by the five central layers. The two extra layers on either side of the central five are introduced to accommodate later rediscrizations (see previous section) which may yield significant values for the strengths of the elements on the extra layers as a result of diffusion. The number of extra layers to be added is specified by considering a diffusion length argument  $L \approx \sqrt{t_{\text{res}}/\alpha}$  where  $t_{\text{res}} = X_{\max}/[0.5(U_1 + U_2)]$  is the average residence time of elements within the computational domain and  $\alpha$  is the thermal (or any other) diffusivity.

External forcing is implemented at the inlet. The forcing signal consists of in-phase components of the most unstable mode of the uniform-density layer and its subharmonic, both at an amplitude  $A_f = A_s = 0.025$ . This forcing leads to early roll-up and pairing of the uniform density layer [5]. Forcing is implemented by displacing elements at the inlet in the cross-stream direction according to the forcing signal.

## 5 Results and discussion

Simulations using a range of the governing physical parameters were obtained and used to analyze the flow and reacting field dynamics [20–22]. In another study the effect the inlet boundary condition was investigated [23]. In this paper we concentrate on the effect of the numerical parameters and we keep the physical parameters fixed.

We consider a shear layer with velocity ratio  $r = U_2/U_1 = 0.5$  and Reynolds (and Pecled) number  $Re = U_1 H/\nu = 12800$ , where  $\nu$  is the kinematic viscosity, evolving in a channel of length  $X_{\max} = 5$ . For the finite reaction rate cases the normalized activation temperature, frequency factor, enthalpy of reaction and mass stoichiometry ratio are  $T_a = E_a/RT_o = 10$ ,  $A_f = A_f H/U_1 = 640$ ,  $Q_o = \Delta h_f/(c_p T_o) = 6$  and  $\phi = 1$  respectively. The Damkohler number,  $Da = \tau_{\text{dif}}/\tau_{\text{che}}$ , where  $\tau_{\text{dif}} = H^2/\alpha$  is the diffusion time scale and  $\tau_{\text{che}} = \frac{T_f}{A_f} \exp(\frac{T_a}{T_f})$  the chemical reaction time scale, and the Karlovitz number,  $Ka = \tau_{\text{che}}/\tau_{\text{flw}}$  where  $\tau_{\text{flw}} = H/U_1$  is the flow time scale, are  $Da \approx 168100$  and  $Ka_d \approx 0.08$ , respectively.

In the simulations the spatial resolution specified via  $h$ ,  $\delta$ , the number of layers and the parameters of the injection-combination scheme was kept invariant. The temporal resolution was increasingly refined to test the convergence of the solution in time. This was carried out for the more general, finite reaction rate case. The time steps considered were  $\Delta t = 0.2, 0.1, 0.05, 0.025$ . Figures 4 and 5 present results from this study. In both figures the  $\Delta t = 0.025$  solution is used as the base-comparison case.

Figure 4 presents the average pointwise error (w.r.t the  $\Delta t = 0.025$  solution) of the velocity,  $\beta$  SZ variable and product mass fraction fields, i.e. the three variables related to the integration of the transport equations, for the three different time-step cases considered, i.e.  $\Delta t = 0.2, 0.1$  and  $0.05$ .

In all cases only the  $0 < x < 4$  section of the computational domain was considered as explained earlier. The solution used in the calculation of the error is obtained on a  $9 \times 51$  mesh, as the average of fifty instantaneous solutions obtained at the same times for all numerical solutions. The figure clearly shows that the solution converges in time and that this convergence is approximately linear.

More detail is offered by Fig. 5, where the profiles for the velocity (top), the  $\beta$  SZ variable (middle) and the product mass fraction (bottom) of the solution obtained as described in the previous paragraph, are presented at the same streamwise location  $x = 2$ . Pictures present the comparison of the  $\Delta t = 0.2$  solutions, with the base,  $\Delta t = 0.025$ , solution. The figure confirms the result of the previous figure. We found that the  $\Delta t = 0.1$  timestep yields solutions which essentially capture most of the features of the more temporally refined solution. As a result, in what follows,  $\Delta t = 0.1$  simulations will be used in the further analysis of the flow.

Figure 6 displays two dimensional visualizations of the instantaneous vorticity ((a)-top) and temperature<sup>12</sup> ((b)-top) for the finite reaction rate flow. These are contrasted to corresponding visualizations of the infinite reaction rate flow (bottom of (a) and (b)).

Substantial similarity is observed between the finite and infinite reaction rate results. The finite reaction rate results suggest that the parameters chosen for the simulations are such that reacting field corresponds to fast (as compared to the flow) reaction, i.e. low Karlovitz number combustion. The infinite reaction rate model describes the extreme of this case, i.e. zero Karlovitz number combustion in which the flame is infinitely thin and cannot be quenched. Thus, under the conditions assumed in the simulations the infinite reaction rate model offers a good approximation of the finite reaction rate flow.

In the context of this discussion the similarity of the finite and infinite reaction rate results is most important in that it offers further validation of the numerical methodology. From a numerical standpoint there are fundamental differences between the finite and infinite reaction rate numerical models (Section 3). Most relevant in this are all parts related to the integration of the product mass fraction equation. This equation is absent in the infinite reaction rate model. Thus, by the simple fact of the similarity of the finite and infinite reaction results a qualitative validation is offered for the numerical integration of the product mass fraction equation, the success of the implementation of the concept of product particles, the new version of the core expansion scheme which includes the inversion of discretization-interpolation function, etc.

A more severe test is demonstrated in Fig. 7 where the instantaneous contribution of the baroclinic torque,  $\dot{\omega}_{\mathbf{B}} = \frac{du}{dt} \times \frac{\nabla \rho}{\rho}$  is plotted for both the finite (top) and infinite (bottom) reaction rate cases. The  $0 < x < 3$  part of the domain is shown. As can be seen from the figure, the characteristics of the field contribution of the baroclinic term of the vorticity equation (Eq. 12) are quite complicated. This should be expected as this quantity represents the rate of change of a gradient field. Satisfactory explanations for it, however, were proposed [20]. Our interest here is the similarity between the finite and infinite reaction rate results. The level of detail in the similarity of such a complicated field substantially increases the confidence in the obtained solution.

More specifically, the density gradient, required in the calculation of  $\dot{\omega}_{\mathbf{B}}$ , is related to the product mass fraction gradient field via the equation of state and the  $\gamma$  SZ variable. As was described in Section 3 the product mass fraction gradient field is obtained using different numerical formulas. The fact that the final result for  $\dot{\omega}_{\mathbf{B}}$  is similar even to the smallest scale, offers a good consistency check between the two approaches.

---

<sup>12</sup>Under the assumptions of the physical model used here the temperature fields are equivalent to those of the product mass fraction.

## 6 Conclusions

The two-dimensional Lagrangian transport element method, an extension of the vortex element method able to resolve reacting scalar transport, has been presented and implemented in the simulation of the non-premixed shear layer flow. The method is able to resolve both the variable density flow and the associated exothermic reacting field.

Results indicate that the method is able to accurately reproduce the essential features of the flow. Convergence of the solution in time is presented and is found to be approximately linear. It is shown that the finite reaction rate solutions obtained correspond to those at low Karlovitz number and bear significant similarity to those of the infinite reaction rate model. This similarity offers validation for the part of the numerical methodology related to the integration of the product mass-fraction equation since this part is not common to the finite and infinite reaction rate models of the reacting field. Examples of this are the utilization of product particles versus product elements for the reaction, the use of alternative formulas for calculating the product mass-fraction gradient and the introduction of a novel version of the core-expansion scheme which does not suffer from the problems associated with earlier versions.

## References

- [1] Anderson, C.R., "A Vortex Method for Flows With Slight Density Variations," *J. Comp. Phys.*, **61**, pp. 417–444, 1985.
- [2] Beale, J.T. and Majda A., "Rates of Convergence for Viscous Splitting of the Navier-Stokes Equations", *Math. Comp.*, **37**, pp. 243–259, 1981.
- [3] Chorin, A.J., "Numerical Study of Slightly Viscous Flow," *J. Fluid Mech.*, **57**, pp. 785–796, 1973.
- [4] Chua, K., Boschitsch, A.H., Koumoutsakos, P., Winckelmans, G. and Leonard, A., "Numerical Simulation of Chemically-Reacting Shear-Layers via Three-Dimensional Fast Particle Methods," AIAA-94-0675 paper, 1994.
- [5] Corcos, G.M. and Sherman, F.S., "The mixing layer: Deterministic Models of a Turbulent Flow. Part 1. Introduction and the Two-Dimensional flow," *J. Fluid Mech.*, **139**, pp. 29–65, 1984.
- [6] Degond, P. and Mas-Gallic, S., "The Weighted Particle Method for Convection-Diffusion Equations. Part 1: The Case of Isotropic Viscosity," *Math. Comp.*, **53 (188)**, pp. 485–507, 1989.
- [7] Ghoniem, A.F., Chorin, A.J. and Oppenheim, A.K., "Numerical Modelling of Turbulent Flow in a Combustion Tunnel," *Phil. Trans. Roy. Soc. London*, **304**, pp. 303–325, 1982.
- [8] Ghoniem, A.F. and Givi, P., "Lagrangian Simulation of a Reacting Mixing Layer at Low Heat Release," *AIAA J.*, **26**, pp. 690–697, 1988.
- [9] Ghoniem, A.F., Heidarinejad, G. and Krishnan, A., "Numerical Simulation of a Thermally Stratified Shear Layer Using the Vortex Element Method," *J. Comp. Phys.*, **79**, pp. 135–166, 1988.
- [10] Ghoniem, A.F. and Krishnan, A., "Origin and Manifestation of Flow-Combustion Interactions in a premixed shear layer," *22nd Symposium (International) on Combustion*, The Combustion Institute, Pittsburgh PA, pp. 665–675, 1988.

- [11] Greengard, C., “The Core Spreading Vortex Method Approximates the Wrong Equation,” *J. Comp. Phys.*, **61**, pp. 345–348, 1985.
- [12] Hald, O.H. and Del-Prete, V.M., “Convergence of Vortex Methods for Euler’s Equations”, *Math. Comp.*, **32**, pp. 791–809, 1978.
- [13] Kempka, S.N. and Strickland, J.H., “A Method to Simulate Viscous Diffusion of Vorticity by Convective Transport of Vortices at a Non-Solenoidal Velocity,” Sandia Laboratory Report SAND93-1763, December, 1993.
- [14] Knio, O.M. and Ghoniem, A.F., “The Three-Dimensional Structure of Periodic Vorticity Layers Under Non-Symmetric Conditions,” *J. Fluid Mech.*, **243**, pp. 353–392, 1992.
- [15] Knio, O.M. and Ghoniem, A.F., “Vortex Simulation of a Three-Dimensional Reacting Shear Layer with Infinite-Rate Kinetics,” *AIAA J.*, **30** (1), pp. 105–116, 1992.
- [16] Krishnan, A. and Ghoniem, A.F., “Simulation of Rollup and Mixing in Rayleigh-Taylor Flow Using the Transport Element Method,” *J. Comp. Phys.*, **99**, pp. 1–27, 1992.
- [17] Lakkis, I., Soteriou, M. and Ghoniem, A.F., “Numerical Simulation of the Dynamics of Large Fire Plumes and the Phenomenon of Puffing,” accepted for publication in the proceedings of the 26th Symposium (International) on Combustion.
- [18] Leonard, A., “Review: Vortex Methods for Flow Simulation”, *J. Comp. Phys.*, **37**, pp. 289–335, 1980.
- [19] Soteriou, M.C. and Ghoniem, A.F., “Effects of the free-stream density ratio on free and forced spatially developing shear layers,” *Phys. Fluids*, **7** (8), pp. 2036–2051, 1995.
- [20] Soteriou, M.C. and Ghoniem, A.F., “The Vorticity Dynamics of an Exothermic Spatially Developing, Forced, Reacting Shear Layer,” *25th Symposium (International) on Combustion*, The Combustion Institute, pp. 1265–1272, 1994.
- [21] Soteriou, M.C. and Ghoniem, A.F. “Dynamics of Reacting Shear Flows; Effects of Exothermicity and Forcing,” AIAA-94-0777 paper, 1994.
- [22] Soteriou, M.C. and Ghoniem, A.F., “On the Application of the Infinite Reaction Rate Model in the Simulation of the Dynamics of Exothermic Mixing Layers,” *Comb. Sci. and Tech.*, **105**, pp. 377–397, 1995.
- [23] Soteriou, M.C. and Ghoniem, A.F., “The Effect of the Inlet Boundary Condition on the Mixing and Burning in an Exothermic Shear Flow,” AIAA-95-0807 paper, 1995.

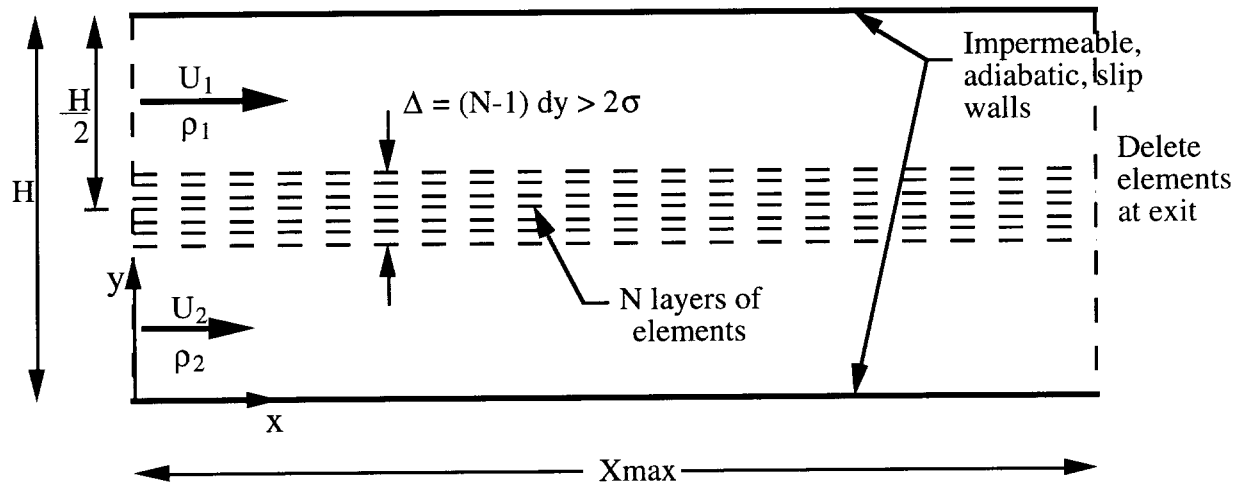


Figure 1: The geometry of the computational domain together with the initial element configuration and some of the boundary conditions.

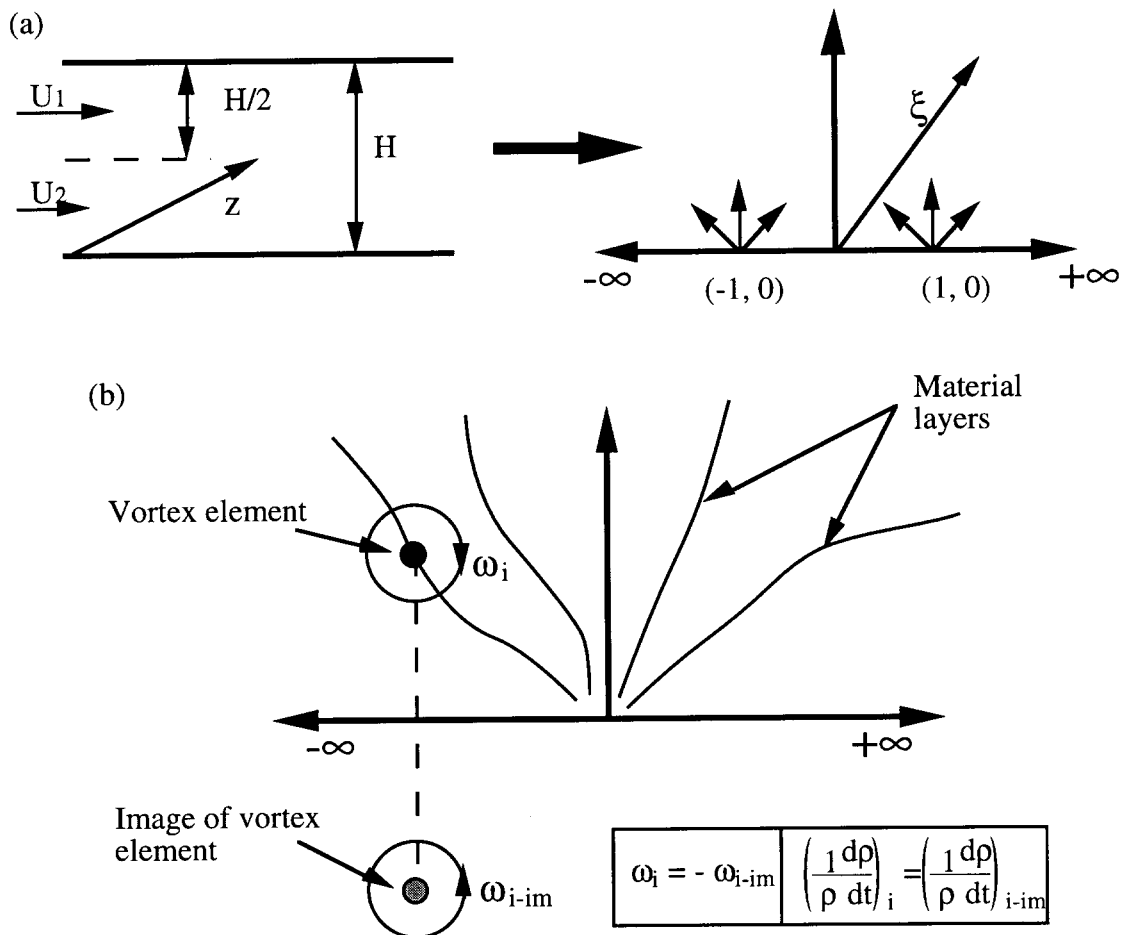


Figure 2: Illustration of the basic features of the Schwarz-Christoffel conformal mapping.

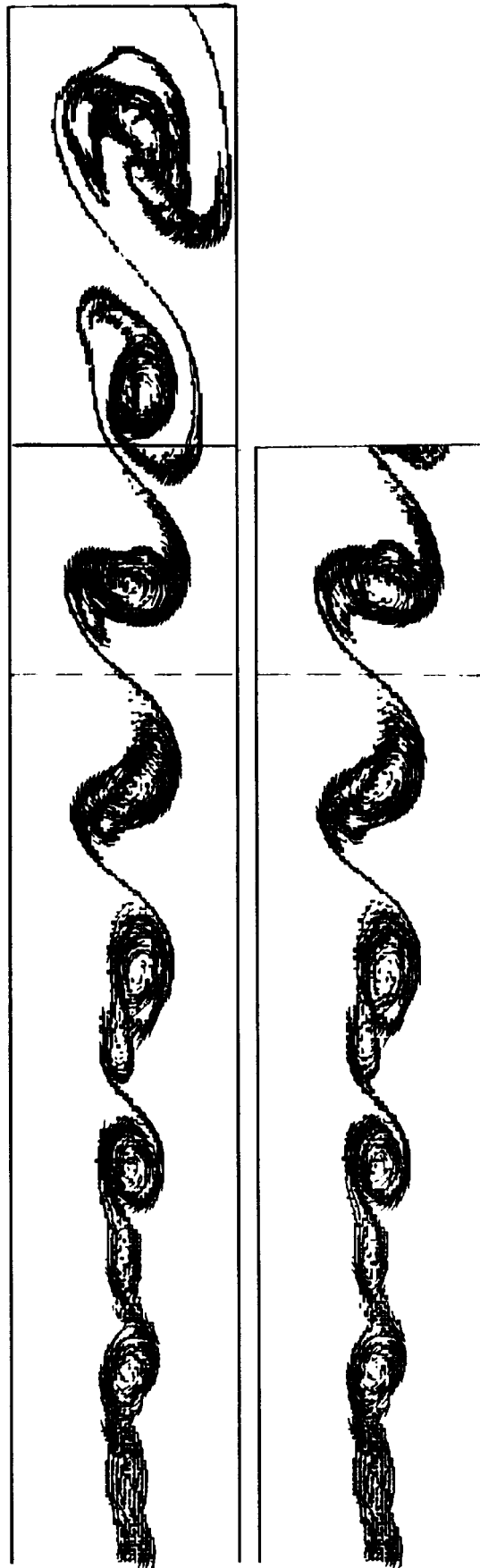


Figure 3: Assessment of the effect of the exit boundary condition by considering increasingly longer computational domains. The shear layer is depicted by plotting the transport elements and their local velocity vectors relative to the average flow. In both simulations the flow is forced, non-exothermic and at  $t = 10$ . The length of the domain is  $X_{\max} = 7$  for the top, and  $X_{\max} = 5$  for the bottom. The dashed lines are at  $x = 4$ .

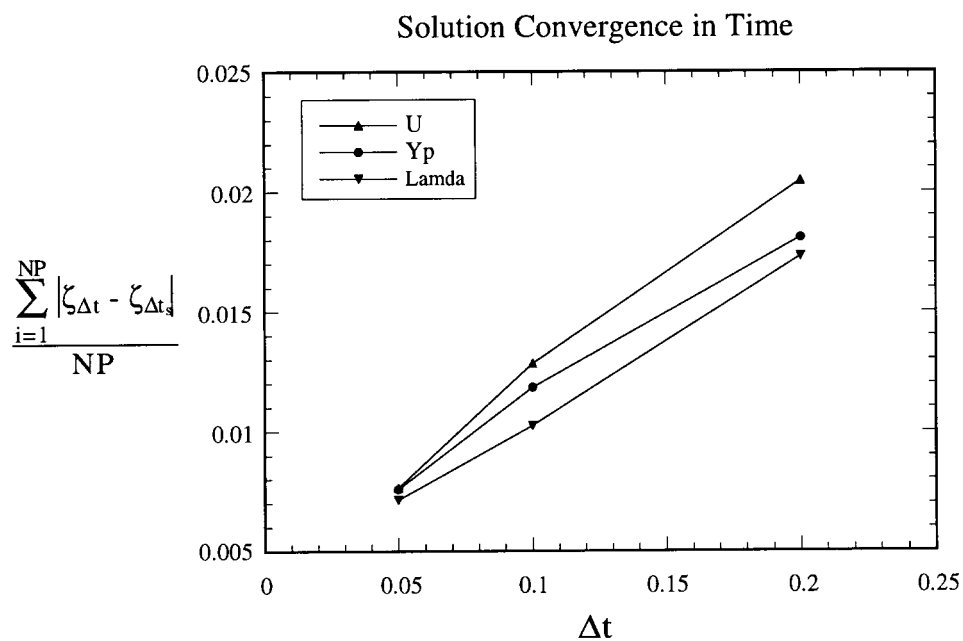


Figure 4: Temporal convergence of solution for the forced, finite reaction rate case with  $X_{\max} = 5$ . Convergence checked by comparing solution with the base  $\Delta t_s = 0.025$  case. The streamwise velocity,  $\beta$  (or  $\lambda$ ) SZ variable and product mass fraction field distributions are investigated, i.e.  $\zeta = u, \beta, Y_p$ . Each solution is established as the average of 50 instantaneous solutions obtained at the same times for all cases, over a  $9 \times 51$  rectangular mesh, i.e.  $NP = 459$ , covering the  $0 < x < 4$ ,  $0 < y < 1$  section of the computational domain.

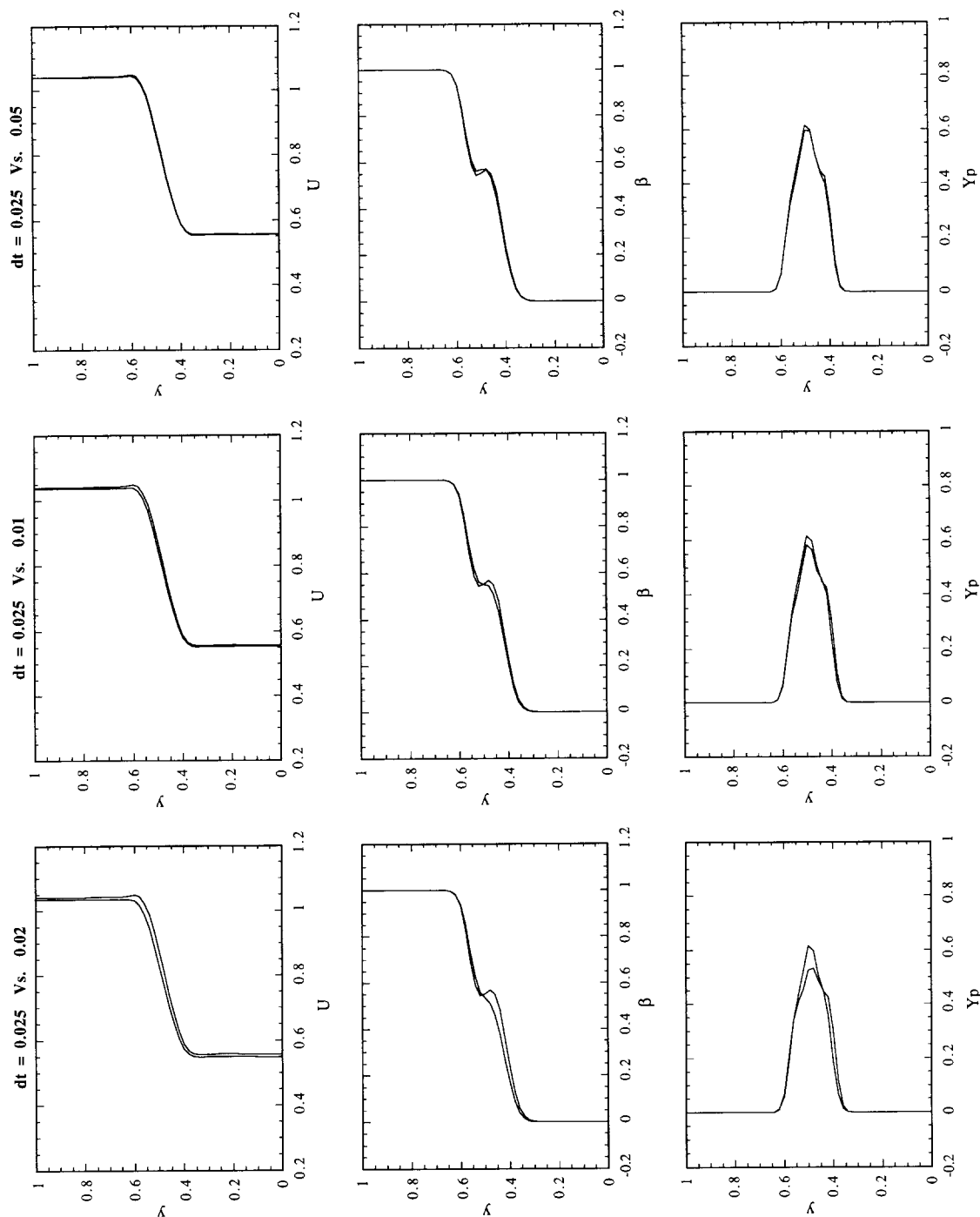


Figure 5: The profiles at  $x = 2$  of the velocity (top),  $\beta$  SZ variable (middle) and product mass-fraction (bottom) for field solutions obtained in the manner described in Fig. 4. The timestep of the solutions decreases from 0.2 to 0.1 to 0.05 from left to right. In each picture the profile is plotted against that of the base  $\Delta t = 0.025$  solution.

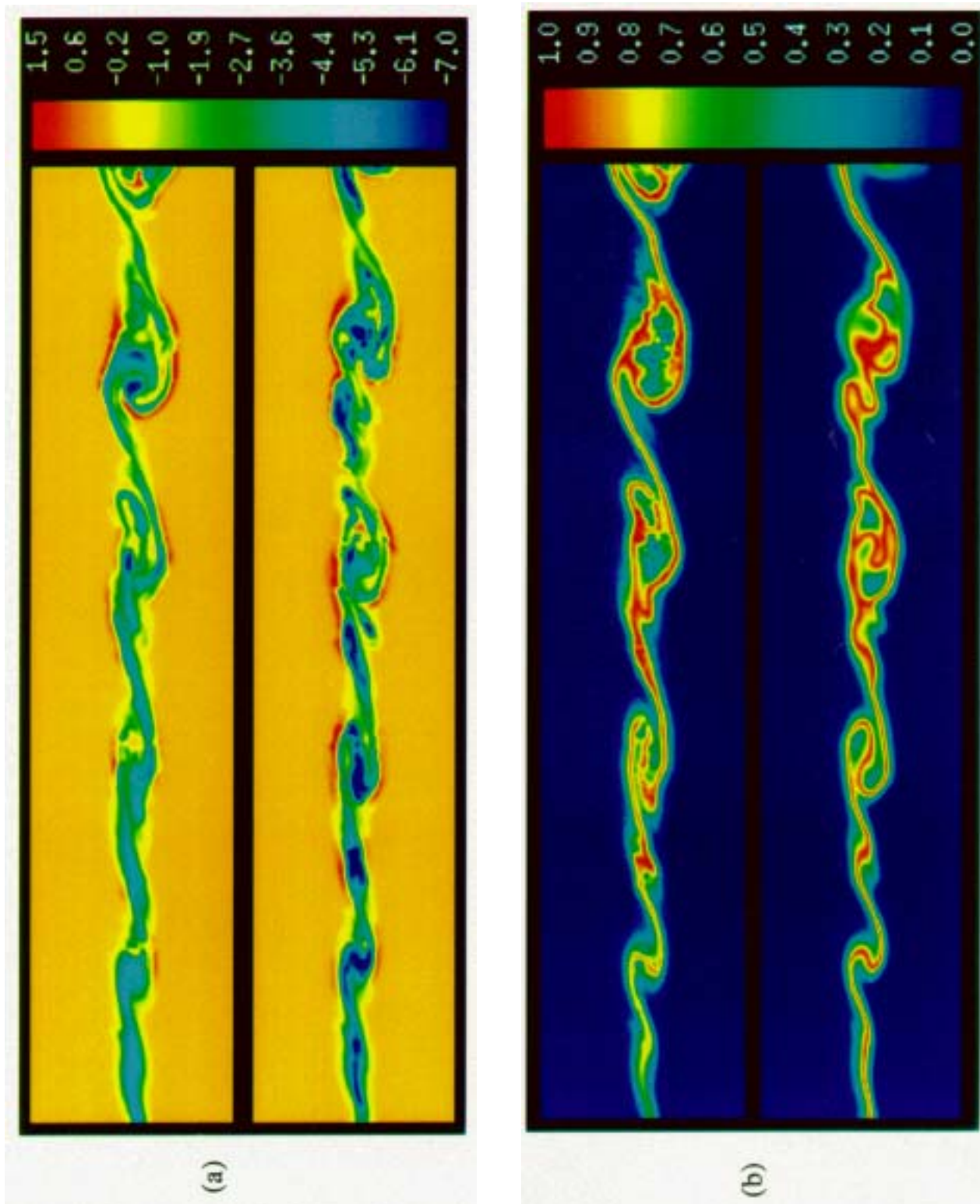


Figure 6: (a) Comparison of the vorticity fields of forced, variable density shear layers with finite (top) and infinite (bottom) reaction rate. Domain shown is  $0 < x < 5$  and  $t = 10$ . (b) The product mass-fraction (or temperature) fields corresponding to the vorticity fields above.

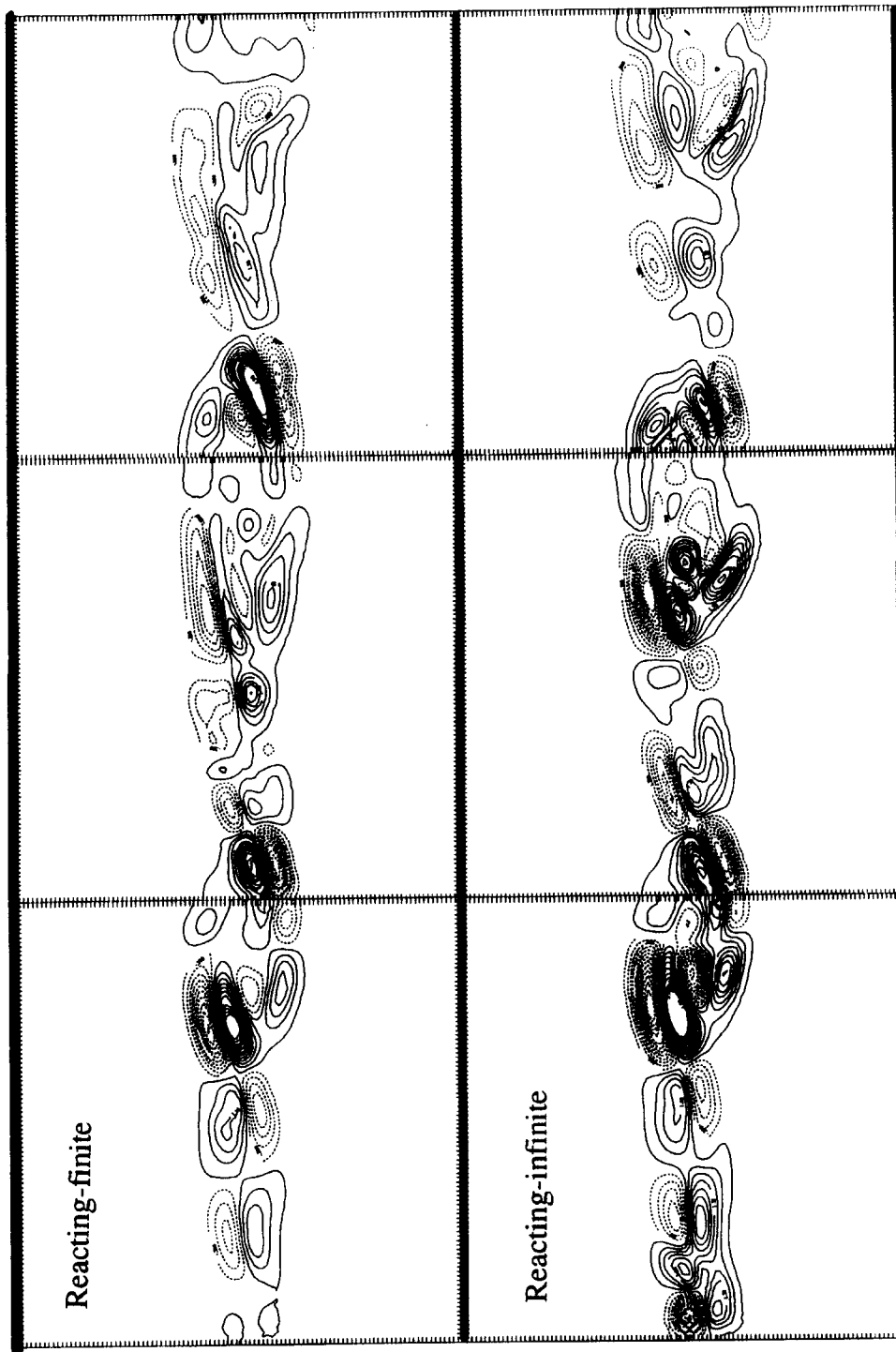


Figure 7: The baroclinic vorticity generation rate of the reacting at finite (top) and infinite (bottom) reaction rate shear layers at time  $t = 10$ . The  $0 < x < 3$  part of the computational domain is shown. Solid/dashed contours indicate negative/positive vorticity at an increment of 0.4.